Fizika Nizkikh Temperatur, 2006, v. 32, Nos. 4/5, p. 411–429

Stripe phases — possible ground state of the high-T_c superconductors

Marcin Raczkowski[1,2], Andrzej M. Oleś[1], and Raymond Frésard[2]

[1] *Marian Smoluchowski Institute of Physics, Jagellonian University*
Reymonta 4, PL-30059 Kraków, Poland
E-mail: A.M.Oles@fkf.mpg.de

[2] *Laboratoire CRISMAT, UMR CNRS-ENSICAEN(ISMRA) 6508,*
6 Bld. du Maréchal Juin Bld., F-14050 Caen, France

Received November 1, 2005

Based on the mean-field method applied either to the extended single-band Hubbard model or to the single-band Peierls-Hubbard Hamiltonian we study the stability of both site-centered and bond-centered charge domain walls. The difference in energy between these phases is found to be small. Therefore, moderate perturbations to the pure Hubbard model, such as next nearest neighbor hopping, lattice anisotropy, or coupling to the lattice, induce phase transitions, shown in the corresponding phase diagrams. In addition, we determine for stable phases charge and magnetization densities, double occupancy, kinetic and magnetic energies, and investigate the role of a finite electron-lattice coupling. We also review experimental signatures of stripes in the superconducting copper oxides.

Pacs: 71.10.Fd, **71.27.+a**, **74.25.−q**, **74.72.−h**

Keywords: high-T_c superconductivity, Hubbard model, stripe phases.

1. Introduction

Since the discovery of high-temperature superconductivity by Bednorz and Müller [1], the unusual physical properties of the copper oxides have stimulated theorists and have led to the appearance of many new ideas [2]. One of the especially appealing new pictures that has emerged is the instability towards a novel type of coexisting incommensurate (IC) charge and magnetic order, i.e., stripe phase. As a rare event in the theory of high temperature superconductivity, the theory preceeded here the experiment and the existence of stripe phases was predicted on the basis of Hartree–Fock (HF) calculations in the two-band model for CuO_2 planes of layered $La_{2-x}Sr_xCuO_4$ (LSCO) [3], before their experimental confirmation. This instability persists as well in the effective single-band Hubbard model [4–7]. All these calculations yielded solutions with a phase separation manifested in formation of nonmagnetic lines of holes, one-dimensional (1D) domain walls or stripes, which separate antiferromagnetic (AF) domains of opposite phases. Such states result from the competition between the superexchange interaction, which stabilize the AF long-range order in the parent Mott insulator, and the kinetic energy of doped holes. Indeed, the magnetic energy is gained when electrons occupy the neighboring sites and their spins order as in the Néel state, whereas the kinetic energy is gained when the holes can move and the AF order is locally suppressed along a domain wall (DW). Thus, a stripe phase provides the best compromise between the superexchange promoting the AF order and the kinetic energy of doped holes.

However, the debate on the microscopic origin of the stripe instability is far from closed. Two main scenarios, based on a Ginzburg–Landau free energy, for the driving mechanism of the stripe phase have been discussed [8,9]. In the first one, stripes are charge-density waves with large periodicity arising from the Fermi surface (FS) instability with the transition being spin driven [3]. A general feature of such

an instability is a gap/pseudogap which opens up precisely on the FS. Hence, the spacing between DWs is equal to $1/x$, with x denoting doping level so as to maintain a gap/pseudogap on the FS. In this scenario spin and charge order occur at the same temperature or charge stripe order sets in only after spin order has developed.

An alternative scenario comes from the Coulomb-frustrated phase separation suggesting that stripe formation is charge driven. Indeed, using the Ising model, it has been shown that the competition between long range Coulomb interactions and short range attraction between holes leads to formation of stripes [10]. In this case Ginzburg–Landau considerations lead to an onset of charge order prior to spin order as the temperature is lowered. However, the above analysis does not take into account spin fluctuations which might be crucial for the nature of the phase transition by precluding the spins from ordering at the charge-order temperature [11]. Moreover, the conjecture that long range Coulomb forces are required to stabilize stripe phases has been challenged by the studies of the t–J model, in which the DW structures were obtained without such interactions [12].

In order to investigate the influence of strong electron correlations due to large on-site Coulomb repulsion U at Cu ions, several methods have been employed to study the stripe phases which go beyond the HF approximation, such as: density matrix renormalization group (DMRG) [12,13], Slave-Boson approximation (SBA) [14–16], variational local ansatz approximation [17], Exact Diagonalization (ED) of finite clusters [18], analytical approach based on variational trial wave function within the string picture [19], dynamical mean field theory (DMFT) [20,21], Cluster perturbation theory (CPT) [22], and quantum Monte Carlo (QMC) [23,24]. In spite of this huge effort, it remains unclear whether DWs are centered on rows of metal atoms, hereafter named site-centered (SC) stripes, or if they are centered on rows of oxygen atoms bridging the two neighboring metal sites, the so-called bond-centered (BC) stripes, and even calculations performed on larger clusters did not yield a definite answer [25]. Therefore, the purpose of this paper is to study the stability of both structures based on the mean-field method applied either to the extended single-band Hubbard model or the single-band Peierls-Hubbard Hamiltonian which includes the so-called static phonons [26]. For stable phases we determine charge and magnetization densities, double occupancy, kinetic and magnetic energies, and investigate the role of a finite electron-lattice coupling.

2. Experimental signatures of stripes

Experimentally, stripe phases are most clearly detected in insulating compounds with a static stripe order, but there is growing evidence of fluctuating stripe correlations in metallic and superconducting materials. The most direct evidence for stripe phases in doped antiferromagnets has come from neutron scattering studies in which charge and spin modulations are identified by the appearance of some IC Bragg peaks, in addition to those which correspond to the crystal structure. However, sometimes sufficiently large crystals are not available for such experiments, and one has to resort to other methods capable of probing local order. These methods include nuclear magnetic resonance (NMR), nuclear quadruple resonance (NQR), muon spin rotation (μSR), scanning tunneling microscopy (STM), and transmission electron microscopy (TEM). Furthermore, angle-resolved photoemission spectroscopy (ARPES), angle-integrated photoemission spectroscopy (AIPES), as well as x-ray photoemission (XPS) and ultraviolet photoemission (UPS) spectroscopies all provide essential information about conspicuous changes in the electronic structure when stripe structure sets in. Finally, a distinct imprint of the 1D spin-charge modulation on transport properties should be detectable as the in-plane anisotropy of the resistivity and the Hall coefficient R_H.

The abundance of the current evidence on various types of stripe order as well as the recent ARPES results on the spectral weight of the cuprate superconductors is contained in the review articles by Kivelson et al. [27], and by Damascelli et al. [28]. Historically, the first compelling evidence for both magnetic and charge order in the cuprates was accomplished in a neodymium codoped compound $La_{2-x-y}Nd_ySr_xCuO_4$ (Nd-LSCO). For $y = 0.4$ and $x = 0.12$, Tranquada et al. [29,30] found that the magnetic scattering is not characterized by the two-dimensional (2D) AF wave vector $(1/2,1/2)$, but by IC peaks at the wave vectors $(1/2 \pm \varepsilon, 1/2)$ with $\varepsilon = 0.118$. Moreover, inspired by the pioneering works demonstrating that the staggered magnetization undergoes a phase shift of π at the charge DWs [3–7], the authors found additional charge order peaks $(\pm 2\varepsilon, 0)$, precisely at the expected position $2\varepsilon = 0.236$. Interestingly, this doping corresponds to a local minimum in the doping dependence of the superconducting temperature T_c in Nd-LSCO [31], suggesting that the static stripes are responsible for this anomalous depression of superconductivity. However, it may well be that the apparent correlation is entirely accidental and therefore the role of stripes in superconductivity remains an open question [2].

Unfortunately, in early studies Tranquada et al. [32] detected only magnetic IC peaks at higher doping levels $x = 0.15$ and $x = 0.2$. Nevertheless, systematic NQR studies of Nd-LSCO revealed the presence of robust charge stripe order throughout the entire superconducting regime of doping $0.07 \le x \le 0.25$ [33]. Also in a more recent study, both charge and spin superlattice peaks at $x = 0.15$ were found recently in the neutron diffraction experiments by Wakimoto et al. [34].

In fact, the reason why static stripes could be detected in this compound is a structural transition from the low temperature orthorhombic (LTO) to the low temperature tetragonal (LTT) phase, induced by the substitution for La ions by isovalent Nd ions. This, in turn, provides a pinning potential for dynamic stripes and stabilizes the charge order. Evidence of a similar pinning potential has also been found both in the μSR and NQR studies of $La_{2-x-y}Eu_ySr_xCuO_4$ (Eu-LSCO) with $y \simeq 0.2$ [35,36]. Moreover, the connection between the LTT phase and the appearance of charge and spin stripe order has been clearly demonstrated both in the neutron scattering and x-ray diffraction studies on $La_{2-x-y}Ba_ySr_xCuO_4$ (Ba-LSCO) with $y = 1/8$ [37,38]. Finally, static IC charge $(2 \pm 2\varepsilon,0)$ and magnetic $(1/2 \pm \varepsilon,1/2)$ peaks have been detected within the LTT phase of $La_{2-x}Ba_xCuO_4$ (LBCO) with $x = 1/8$ [39]. The position of the peaks and the established incommensurability $\varepsilon = 0.118$ are exactly the same as those obtained by Tranquada et al. [30] for Nd-LSCO. Notably, the peaks that correspond to charge order appear always at somewhat higher temperature than the magnetic ones, indicating that the stripe order is driven by the charge instability.

Let us now discuss the experimental evidence of slowly fluctuating stripes in $La_{2-x}Sr_xCuO_4$. The main difference between the Ba and Sr codoped system is the fact that the latter undergoes a structural phase transition from the high-temperature tetragonal (HTT) phase to the LTO phase. As a consequence, in the superconducting regime $x \ge 0.06$, the LSCO system exhibits purely *dynamic* magnetic correlations which give rise to IC peaks at the wave vector $(1/2 \pm \varepsilon,1/2)$ specified in tetragonal lattice units $2\pi/a_{\text{tetra}}$. In their seminal inelastic neutron scattering studies, Yamada et al. [40] established a remarkably simple relation $\varepsilon \simeq x$ for $0.06 \le x \le 0.12$, followed by a lock-in effect at $\varepsilon \simeq 1/8$ for larger x.

In contrast, in the insulating spin-glass regime of LSCO $x \le 0.06$, quasielastic neutron scattering experiments with the main weight at zero frequency demonstrate that IC magnetic peaks are located at the wave vectors $(1/2 \pm \varepsilon/\sqrt{2},1/2 \pm \varepsilon/\sqrt{2})$ [41–43]. This phenomenon has often been interpreted as the existence of static diagonal stripes, even though no signatures of a charge modulation were observed. Another possible explanation is the formation of a short ranged spiral order as its chirality also breaks the translational symmetry of the square lattice by a clockwise or anticlockwise twist [44]. Remarkably, even though the spin modulation changes from a diagonal to vertical/horizontal one, i.e., along Cu–O bonds, at x around 0.06, ε follows the doping x reasonably well over the entire range $0.03 \le x \le 0.12$, as shown in Fig. 1. In fact, just for $x = 0.06$, both diagonal ($\varepsilon = 0.053$) and vertical/horizontal ($\varepsilon = 0.049$) IC spin modulations have been found to coexist [43]. In a stripe model this corresponds to a constant density of 0.5 (0.7) holes per Cu atom in the DWs in the vertical/horizontal (diagonal) stripe phases, respectively, because of the difference in Cu spacings in the two geometries, i.e., $a_{\text{ortho}} = \sqrt{2}a_{\text{tetra}}$. In contrast, in the narrow region $0.02 \le x \le 0.024$, IC magnetic peaks are located at the wave vector $(1/2 \pm \varepsilon/2,1/2 \pm \varepsilon/2)$ with $\varepsilon \simeq x$ corresponding to a constant charge of one hole/Cu ion along a diagonal DW [45–47]. However, below $x = 0.02$, this does not hold anymore and the incommensurability gets locked with the value $\varepsilon \simeq 0.014$.

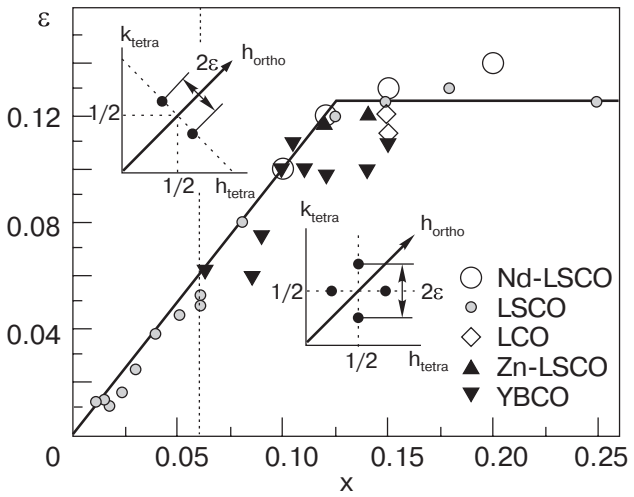

Fig. 1. Summary of experimental data illustrating the doping dependence of incommensurability ε in the cuprates. Results have been obtained by different groups: Nd-LSCO (Refs. 29–32); LSCO (Refs. 40–43,45–47); LCO (Ref. 51); Zn-LSCO (Refs. 52,53); YBCO (Refs. 54,55). In LSCO, ε has been defined as a distance from the IC peak position to the AF wave vector (1/2,1/2) either in the orthorhombic ($x < 0.06$) or tetragonal ($x > 0.06$) notation (see insets), whereas at $x = 0.06$, both definitions are used due to the coexistence of diagonal and parallel to the Cu–O bonds spin modulations.

Unfortunately, any concomitant charge ordering has not yet been detected in LSCO. Nevertheless, by comparing the data based on the wipeout effect of ^{63}Cu NQR charge order parameter in LSCO with the ones obtained from charge stripe compounds as (Nd,Eu,Ba)-LSCO, Hunt et al. [48] concluded that a similar stripe instability exists in LSCO over the whole underdoped superconducting region $1/16 \le x \le 1/8$. It is also worth mentioning that a very compiling evidence for its existence has been established in the measurements of the in-plane resistivity and the dynamical infrared conductivity anisotropy [49,50].

Experimental detection of IC magnetic peaks in the LTO phase of LSCO suggests that the LTT structure is not essential for the appearance of stripes. This conjecture has been confirmed in experiments on the oxygen doped $La_2CuO_{4+\delta}$ (LCO) with the orthorhombic crystal structure [51]. It is also supported by the evidence for *static* IC magnetic peaks in another orthorhombic compound $La_{2-x}Sr_xCu_{1-y}Zn_yO_4$ (Zn-LSCO) with y up to 0.03, even though attempts to observe the charge order peaks were unsuccessful [52,53]. In fact, Zn substitution pins the stripe fluctuations similarly to the rare-earth elements. However, in contrast to the latter, it does not induce a structural transition to the LTT phase, but provides randomly distributed pinning centers that promote meandering of stripes and correspondingly broadens IC peaks.

An important question is whether charge stripes appear solely in monolayered lanthanum compounds or if they are a generic feature of all the cuprates. The latter conjecture seems to be supported by inelastic neutron scattering experiments on bilayered $YBa_2Cu_3O_{6+\delta}$ (YBCO) compounds that have identified the presence of IC spin fluctuations throughout its entire superconducting regime [54]. In fact, as the doped charge is nontrivially distributed between the CuO_2 planes and CuO chains, it is very difficult to determine the precise doping level x in the CuO_2 sheet of YBCO. Nevertheless, systematic studies by Dai et al. [54] have shown that the incommensurability in YBCO increases initially with doping but it saturates faster than in LSCO, i.e., already at $x \simeq 0.1$ with the value $\varepsilon \simeq 0.1$. Unfortunately, there is no any compelling explanation that would account for such a different behavior of ε in both systems. Eventually, charge order peaks have been observed in $YBCO_{6.35}$ but in spite of several attempts, no static charge order could be detected in $YBCO_{6.5}$ and $YBCO_{6.6}$ so far [55].

Furthermore, although some neutron scattering experiments have been performed on $Bi_2Sr_2CaCu_2O_{8+\delta}$ (BSCCO) sample, the sample has only produced weak evidence of the IC structure [56]. In contrast, Fourier transform of the recent STM data has revealed some IC peaks corresponding to a four-period modulation of the local density of states along the Cu–O bond direction, which may imply the existence of stripes [57]. Nevertheless, definite answer pertinent to the appearance of stripes in all the cuprates remains still unsettled and further experiments are required to reach an unambiguous conclusion, even though the summary of the experimental data illustrating the doping dependence of the incommensurability ε in cuprates, depicted in Fig. 1, includes an array of compounds.

Tendency towards phase separation is also a starting point to understand the doping evolution of the electronic structure in LSCO and Nd-LSCO. For example, ARPES spectra measured at the $X = (\pi, 0)$ point in LSCO show that even though the data are solely characterized by a single high binding energy feature in the insulating regime, upon increasing doping one observes a systematic transfer of spectral weight from the high- to the low binding energy part [58]. Consequently, a well-defined quasiparticle (QP) peak develops near the optimal doping. In contrast, the intensity near the $S = (\pi/2, \pi/2)$ point remains suppressed for the entire underdoped regime so that a QP peak is observed only for $x \ge 0.15$.

Another peculiar feature of the ARPES band dispersion is extensively discussed in the literature saddle point at the X point, the so-called flat band [59]. As hole doping increases, the flat band moves monotonically upwards and crosses the Fermi level E_F at $x \simeq 0.2$. This is reflected in the enhancement of the DOS at the chemical potential $N(\mu)$ observed by AIPES [60].

The experimental distribution of the photoemission spectral weight near the X and S points in doped LSCO has been nicely reproduced using the DMFT approach for vertical SC stripes obtained within the Hubbard model [20]. As a consequence of the stripe order, the obtained spectra along the Γ–X–M path were not equivalent to those along the Γ–Y–M one, with $\Gamma = (0,0)$ and $Y = (0, \pi)$. Moreover, as in the experiment, the spectral weight along the Γ–X direction was suppressed close to the Γ point and simultaneously enhanced at the X point. Furthermore, in the framework of stripes, the flat QP band near the X point with a large intensity at the maximum below the chemical potential μ follows from a superposition of the dispersionless 1D metallic band along the x direction, formed by holes propagating along the vertical domain walls, and an insulating band that stems from the AF domains. In contrast, an AF band at the Y point is characterized by a high binding energy well below μ and consequently the spectral weight at $\omega = \mu$ al-

most vanishes. Finally, a distinct gap for charge excitations should open at μ near the S point. This gap follows indeed from the stripe structure — while the system may be metallic along the stripes, i.e., in the antinodal directions $\Gamma-X$ or $\Gamma-Y$, the low-energy excitations should be noticeably suppressed along the nodal direction $\Gamma-S$ crossing all the stripes. This conjecture is also supported either by the ED studies [18] or by the analytical approach based on variational trial wave function within the string picture [19], both applied to the t–t'–t''–J model, or by the CPT for the t–J model [22].

In fact, the low-energy spectral weight of Nd-LSCO at $x = 0.12$, a model compound for which the evidence of spin and charge stripe order is the strongest, is also mostly concentrated in flat regions along the $\Gamma-X$ and $\Gamma-Y$ directions, while there is only little spectral weight along the $\Gamma-S$ direction [61]. On the other hand, ARPES spectra of both LSCO and Nd-LSCO at $x = 0.15$ have revealed not only the presence of flat bands around the X and Y points, but also the existence of appreciable spectral weight at E_F in the nodal region [62]. While the observation of flat segments might be directly ascribed to 1D domain walls [63], detection of nodal spectral weight poses a formidable task to develop a theory that would describe the electronic structure resembling the FS of a fully 2D system because, as it was already stressed out, the nodal spectral weight is expected to be suppressed in a static SC stripe picture [18–20,22]. Indeed, the experimentally established FS looks rather like the one arising from disorder or from dynamically fluctuating stripes [63].

Alternatively, guided by the CPT results showing that while the SC stripes yield little spectral weight near the nodal region, the BC ones reproduce quite well the nodal segments [22], Zhou et al. [62] have conjectured that the experimental FS may result from the coexistence of the SC and BC stripes. Within this framework, upon increasing doping the BC stripes are formed at the expense of the SC ones. This scenario is particularly interesting because it has been shown that the BC stripe, in contrast to its SC counterpart, enhances superconducting pairing correlations [64]. The relevance of a bond order at the doping level $x = 0.15$ is supported by recent studies of the ARPES spectra in a system with the BC stripes [65]. These studies have yielded pronounced spectral weight both in the nodal and antinodal directions, reproducing quite well the experimental results in Nd-LSCO and LSCO [62]. Furthermore, the stripe scenario would also explain the origin of the already discussed two components seen in the ARPES spectra at the X point near $x = 0.05$ [58]. Indeed, the response from the AF insulating regions would be pushed to the high binding energies due to the Mott gap, whereas the charge stripes would be responsible for the other component near E_F.

Existence of DWs should also give rise to the appearance of new states inside the charge-transfer gap that would suppress the shift of the chemical potential μ in the underdoped regime $x < 1/8$ where ε increases linearly. Such pinning of μ in LSCO was indeed deduced from XPS experiments [66]. In contrast, in the overdoped region with a lock-in effect of ε, the number of stripes per unit cell saturates, doped holes penetrate into the AF domains, and consequently μ would move fast with doping in agreement with the experimental data. The picture of broadened stripes and holes spreading out all over the AF domains above $x = 1/8$ is also indicated by the doping dependence of the resistivity and the Hall coefficient R_H in Nd-LSCO. Namely, a rapid decrease in the magnitude of R_H for doping level $x \le 1/8$ at low temperature provides evidence for the 1D charge transport, whereas for $x > 1/8$, relatively large R_H suggests a crossover from the 1D to 2D charge transport [67]. Altogether, it appears that the metallic stripe picture does capture the essence of the low-lying physics for Nd-LSCO and LSCO systems.

Conversely, it is important to note that so far no evidence of IC peaks has been detected in any electron-doped cuprates superconductors. Instead, the neutron scattering experiments have established only *commensurate* spin fluctuations as in $Nd_{2-x}Ce_xCuO_4$ (NCCO), both in the superconducting and in normal state [68]. Moreover, observation of such peaks is consistent with the XPS measurements in NCCO showing that the chemical potential increases monotonously with electron doping [69].

3. Numerical results

In this Section we attempt a systematic investigation of the properties and relative stability of filled vertical and diagonal stripes. We shall see that in spite of the difficulty to stabilize the ground state with half-filled stripes (one hole per every two atoms in a DW), the mean-field framework is useful as providing a generic microscopic description of filled inhomogeneous reference structures with the filling of one doped hole per stripe unit cell. Their special stability rests on a gap that opens in the symmetry broken state between the highest occupied state of the lower Hubbard band and the bottom of the so-called mid-gap bands, i.e., some additional unoccupied bands lying within the Mott-Hubbard gap that are formed due to holes propagating along DWs [26].

Here, we extend early HF studies of the filled DWs [4–7] and determine a phase diagram of the Hubbard

model with an anisotropic nearest-neighbor hopping t by varying the on-site Coulomb repulsion U and investigating locally stable structures for representative hole doping levels $x = 1/8$ and $x = 1/6$. We also report the changes in stability of the stripe structures in the extended Hubbard model due to the next-neighbor hopping t' and to the nearest neighbor Coulomb interaction V. Finally, in order to gain a comprehensive understanding of the competition between different types of stripes in a realistic model, we include lattice degrees of freedom induced by a static Peierls electron-lattice coupling.

3.1. Extended single-band Hubbard model

The starting point for the analysis of stripe structures is the extended single-band Hubbard model, which is widely accepted as the generic model for a microscopic description of the cuprate superconductors [70],

$$H = -\sum_{ij\sigma} t_{ij} c^{\dagger}_{i\sigma} c_{j\sigma} + U \sum_{i} n_{i\uparrow} n_{i\downarrow} + V \sum_{\langle ij \rangle} n_i n_j \ , \quad (1)$$

where the operator $c^{\dagger}_{i\sigma}$ ($c_{j\sigma}$) creates (annihilates) an electron with spin σ on lattice site i (j), and $n_i = c^{\dagger}_{i\uparrow} c_{i\uparrow} + c^{\dagger}_{i\downarrow} c_{i\downarrow}$ stands for the electron density. The hopping t_{ij} is t on the bonds connecting nearest neighbors sites $\langle i, j \rangle$ and t' for second-neighbor sites, while the on-site and nearest neighbor Coulomb interactions are, respectively, U and V.

The model can be solved self-consistently in real space within the HF, where the interactions are decoupled into products of one-particle terms becoming effective mean fields that act on each electron with the same strength. This approximation basically involves solving an eigenvalue problem. The obtained wavefunctions form a new potential and hence the Hamiltonian for a new eigenvalue problem. Typically, the new potential is chosen as some linear combination of the current and preceding potential. The iterations are continued until the input and output charge density and energy do not change within some prescribed accuracy. The most significant drawback of this method is that it neglects correlations. Electron correlation changes the system properties and manifests itself in the decrease of the ground state energy. The difference between the energy of the exact ground state and the energy obtained within the HF is thus called the correlation energy. It arises from the fact that an electron's movement is correlated with the electrons around it, and accounting for this effect lowers further the energy, beyond the independent electron approximation.

We do not consider noncollinear spin configurations, and use the most straightforward version of the HF with a product of two separate Slater determinants for up and down spins, whence,

$$n_{i\uparrow} n_{i\downarrow} \simeq n_{i\uparrow} \langle n_{i\downarrow} \rangle + \langle n_{i\uparrow} \rangle n_{i\downarrow} - \langle n_{i\uparrow} \rangle \langle n_{i\downarrow} \rangle . \quad (2)$$

A similar decoupling is performed for the nearest neighbor Coulomb interaction. Calculations were performed on 12×12 (16×16) clusters for $x = 1/6$ ($x = 1/8$) with periodic boundary conditions, and we obtain stable stripe structures with AF domains of width five atoms for $x = 1/6$ and seven atoms for $x = 1/8$. Typical solutions at $x = 1/8$ are shown in Fig. 2 with the local hole density,

$$\langle n_{hi} \rangle = 1 - \langle n_{i\uparrow} + n_{i\downarrow} \rangle , \quad (3)$$

scaled by the diameter of the black circles and the length of the arrows being proportional to the amplitude of local magnetization density,

$$\langle S^z_i \rangle = \frac{1}{2} \left| \langle n_{i\uparrow} - n_{i\downarrow} \rangle \right| . \quad (4)$$

These structures possess nonmagnetic DWs with enhanced hole density which separate AF domains having hole density almost unchanged with respect to the undoped case. Note that the AF sites on each side of the DWs have a phase shift of π.

In order to appreciate better the microscopic reasons of such arrangement let us consider a small cluster consisting of three atoms filled by two electrons and one hole (with respect to half-filling with the

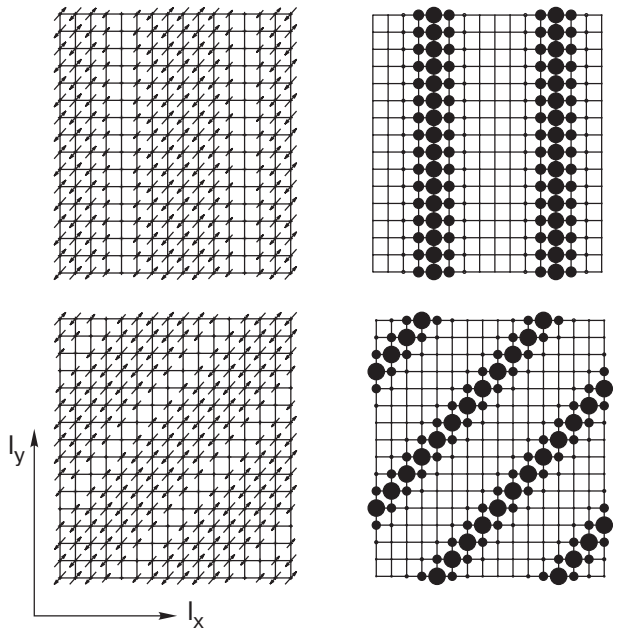

Fig. 2. Vertical site-centered (VSC) and diagonal site-centered (DSC) stripe phases as found for $U/t = 5$ at hole doping $x = 1/8$. The length of arrows is proportional to the magnetization $\langle S^z_i \rangle$ and the hole density $\langle n_{hi} \rangle$ is scaled by the diameter of black circles.

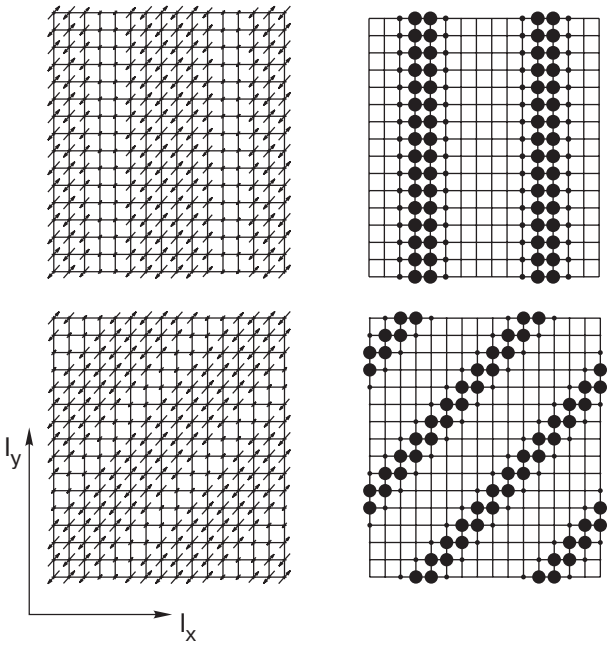

Fig. 3. Vertical bond-centered (VBC) and diagonal bond-centered (DBC) stripe phases as found for $U/t = 5$ at hole doping $x = 1/8$. The meaning of the arrows and black circles as in Fig. 2.

electron density $n = 1$ per site). For simplicity we assume that the electrons are confined to the considered cluster owing to large Coulomb interaction $U >> t$, and we do not take into account any interactions with the AF background. There are two possible candidates for the ground state. The first one corresponds to a hole added to three atoms of a single AF domain in which, if we suppose that a $\downarrow$-spin electron is replaced by a hole, the two remaining $\uparrow$-spin electrons can be found in one of three allowed configurations: $\{\uparrow,0,\uparrow\}$, $\{\uparrow,\uparrow,0\}$, and $\{0,\uparrow,\uparrow\}$ (the other configurations are excluded by the Pauli principle). Hence, this polaronic state gives the total energy,

$$E_P = -\sqrt{2}t\,, \tag{5}$$

and the Coulomb interaction U does not contribute.

A different situation is obtained when a hole occupies instead a DW separating two AF domains. Delocalization leads then to similar three configurations to those obtained above with opposite spins: $\{\uparrow,0,\downarrow\}$, $\{\uparrow,\downarrow,0\}$, and $\{0,\uparrow,\downarrow\}$, but in addition, three configurations with one doubly occupied site $\{\uparrow\downarrow,0,0\}$, $\{0,\uparrow\downarrow,0\}$, and $\{0,0,\uparrow\downarrow\}$, can be reached as excited states which cost Coulomb energy U. Moreover, three other configurations with interchanged $\uparrow$- and $\downarrow$-spins are then also accessible via the decay of double occupancies: $\{\downarrow,0,\uparrow\}$, $\{\downarrow,\uparrow,0\}$, and $\{0,\downarrow,\uparrow\}$. In the regime of large U, the total energy in the ground state can be found in a perturbative way, and as a result one obtains,

$$E_S = -\sqrt{2}t - \frac{4t^2}{U}\,. \tag{6}$$

Therefore, the Hilbert space for the latter solitonic solution is larger and one finds that this solution is always more stable than the polaronic one [26]. The argument applies also to 2D systems, where the DWs are more stable than the lines of polarons in an AF background.

We compare the stability of such nonmagnetic SC domain walls with the BC stripe phases in which DWs are formed by pairs of magnetic atoms, as obtained by White and Scalapino [12] (cf. Fig. 3). In the three-band model, SC (BC) stripes correspond to DWs centered at metal (oxygen) sites, respectively [71–74].

3.2. Effect of hopping anisotropy

We begin by setting $t' = 0$ and $V = 0$ with the goal of elucidating the effects of hopping anisotropy on the stripes. This is motivated by the fact that the first detection of static stripes in both charge and spin sectors was accomplished in Nd-LSCO [29] indicating that rare-earth elements doping is in some way helpful for pinning the stripe structure. Indeed, it produces a structural transition in the system from the LTO to LTT phase [75]. Both phases involve a distortion of the CuO_2 plane by rotation of the CuO_6 octahedra. In the LTO phase the tilt axis runs diagonally within the copper plane, such that all the oxygen atoms are displaced out of the plane. Conversely, in the LTT phase this rotation takes place around an axis oriented along the planar Cu–O bonds. Therefore, oxygen atoms on the tilt axis remain in the plane, while the ones in the perpendicular direction are displaced out of the plane. This provides a microscopic origin for in-plane anisotropies — the Cu–Cu hopping amplitude t depends on the Cu–O bond and it is isotropic in the LTO phase and anisotropic in the LTT one. For a physical tilt angle of order 5°, the relative anisotropy taking $t_y < t_x$,

$$\varepsilon_t = \frac{|t_x - t_y|}{t_y}\,, \tag{7}$$

is weak and amounts to $\varepsilon_t = 0.015$ [76,77]. The direction with a larger hopping amplitude coincides with the direction of a stronger superexchange coupling J.

The possible relationship between this anisotropy and the onset of stripe phases has been intensively studied within anisotropic Hubbard ($t_x \neq t_y$) or t-J ($t_x \neq t_y$, $J_x \neq J_y$) models by means of various techniques: unrestricted HF approach [76], DMRG [77], and QMC method [23]. The in-plane anisotropies might also be represented theoretically by on-site po-

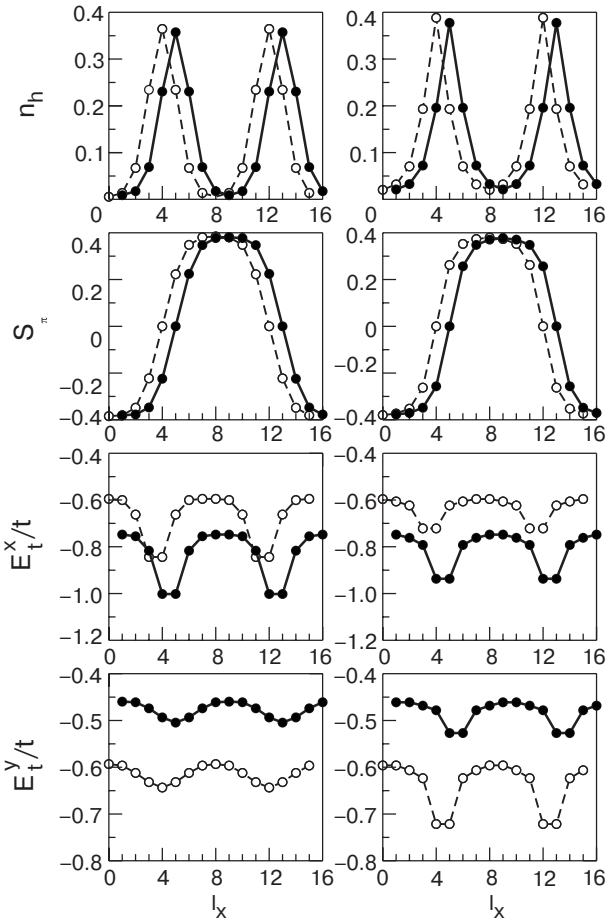

Fig. 4. Local hole $n_h(l_x)$ (top) and magnetization $S_\pi(l_x)$ (second row) density; kinetic energy $E_t^x(l_x)$ (third row) and $E_t^y(l_x)$ (bottom) projected on the bonds in the x-(y)-directions, respectively, of the VSC (left) and DSC (right) stripe phases shown in Fig. 2 (open circles) as well as of the ones obtained in the anisotropic model with $t_x/t_y = 1.22$ (filled circles). For clarity, the latter are shifted by one lattice constant from the origin of the coordinate system.

tentials as in the QMC study by Riera [24]. All these investigations have shown a pronounced tendency to forming stripe phases, which manifests itself by the reduction of their energy [76,77], accompanied by the appearance of IC peaks in the spin and charge structure factor [23,24]. It appears that a finite anisotropy of the next-nearest neighbor hopping term t' might play a role in stabilizing diagonal incommensurate peaks observed in the spinglass phase of LSCO ($0.02 \le x \le 0.06$) [41–43,45–47]. Indeed, although the LTO phase is usually considered as isotropic, which is the case for nearest neighbor hopping and interaction, a different length of the orthorhombic axes implies the need for an anisotropic t' parameter. Exact diagonalization studies incorporating such anisotropy have shown that it strongly amplifies hole correlations along one direction and suppresses them along the other, resulting in a 1D pattern of holes [78].

It turns out, however, that the variation of the hopping anisotropy ε_t (7) has only a little visible effect on the local hole density,

$$n_h(l_x) = 1 - \langle n_{(l_x,0),\uparrow} + n_{(l_x,0),\downarrow} \rangle , \qquad (8)$$

shown in Fig. 4 as a function of the x-direction coordinate l_x for a given y-direction coordinate $l_y = 0$, even at the unrealistically large anisotropy level $\varepsilon_t = 0.22$, corresponding to $t_x/t = 1.1$ and $t_y/t = 0.9$. Similarly, the anisotropy does not modify the modulated magnetization density,

$$S_\pi(l_x) = (-1)^{l_x} \frac{1}{2} \langle n_{(l_x,0),\uparrow} - n_{(l_x,0),\downarrow} \rangle ,$$

with a site dependent factor $(-1)^{l_x}$ compensating modulation of the staggered magnetization density within a single AF domain.

In contrast, the strong effect of finite anisotropy ε_t (7) is clearly demonstrated by variation of the expectation values of the bond hopping terms along the x- and y-directions,

$$E_t^x(l_x) = -t_x \sum_\sigma \langle c^\dagger_{(l_x,0),\sigma} c_{(l_x+1,0),\sigma} + \text{h.c.} \rangle , \quad (10)$$

$$E_t^y(l_x) = -t_y \sum_\sigma \langle c^\dagger_{(l_x,0),\sigma} c_{(l_x,1),\sigma} + \text{h.c.} \rangle . \quad (11)$$

These features are seen in Fig. 4. For the VSC stripes one finds a large anisotropy in the values of the kinetic energies (10) and (11), which becomes especially pronounced beside the stripes, and is strongly reinforced by the hopping anisotropy. Therefore, taking into account that the hopping between two different charge densities is favored over motion between equal densities, one should expect that transverse charge fluctuations will always tune the direction of DWs along the weaker hopping direction in the anisotropic model. Analogous conclusion based on Fig. 5 might be drawn concerning the orientation of the VBC stripes.

Regarding diagonal stripes, although a finite anisotropy in hopping is also reflected in the kinetic energy anisotropy, a system with either the DSC or DBC stripe pattern becomes topologically frustrated and consequently may gain less kinetic energy compared to a system with vertical stripes, taking a full advantage of the hopping anisotropy (cf. Tables 1 and 2).

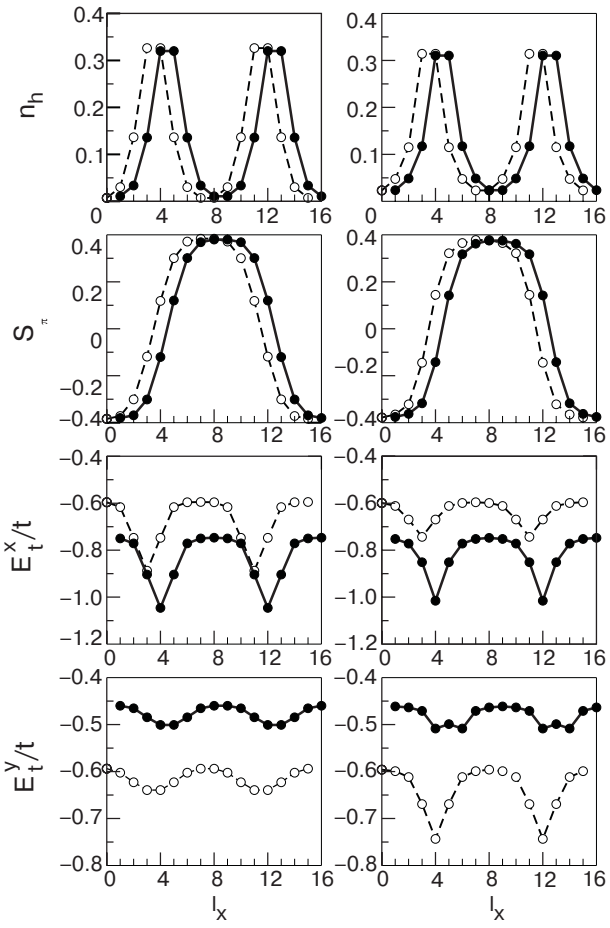

Fig. 5. The same as in Fig. 4 but for the BC stripe phases shown in Fig. 3.

Table 1. Site-normalized ground-state energy $E_{\rm tot}$, kinetic energy (E_t^x, E_t^y), and potential energy E_U in the isotropic Hubbard model with $U/t = 5$ and $x = 1/8$ as obtained for different stripe phases: vertical site-centered (VSC), diagonal site-centered (DSC), vertical bond-centered (VBC) and diagonal bond-centered (DBC). In the HF, both types of vertical stripes are degenerate.

	E_t^x/t	E_t^y/t	E_U/t	$E_{\rm tot}/t$
VB(S)C	−0.6753	−0.6147	0.4900	−0.8000
DBC	−0.6375	−0.6375	0.4726	−0.8024
DSC	−0.6368	−0.6368	0.4696	−0.8040

Table 2. The same as in Table 1 but with the hopping anisotropy $\varepsilon_t = 0.22$.

	E_t^x/t	E_t^y/t	E_U/t	$E_{\rm tot}/t$
DBC	−0.8143	−0.4807	0.4815	−0.8135
DSC	−0.8098	−0.4836	0.4793	−0.8141
VB(S)C	−0.8304	−0.4776	0.4938	−0.8142

The effect of an increasing anisotropy illustrates the phase diagram shown in Fig. 6 determined by varying U and the ratio t_x/t_y of the nearest-neighbor hoppings in the x- and y-directions, while maintaining constant $t = (t_x + t_y)/2$. We observe the generic crossover from vertical to diagonal stripes with increasing Coulomb interaction reported in early HF studies [4–7]. The transition from the VSC to DSC stripes appears in the isotropic case at $U/t \simeq 4.1$ for $x = 1/8$, and at a higher value $U/t \simeq 4.6$ for $x = 1/6$ (cf. Fig. 6,*a*). The corresponding phase boundary between the VBC and DBC stripes is shifted towards stronger Coulomb interaction and occurs at $U/t \simeq 4.4$ (5.0) for $x = 1/8$ ($x = 1/6$), respectively (cf. Fig. 6,*b*).

The results shown in Fig. 6 have a simple physical interpretation. Stripe phases occur as a compromise between, on the one hand, the AF interactions between magnetic ions and the local Coulomb interactions responsible for charge localization, and the kinetic energy of doped holes which on the contrary favors charge delocalization. The kinetic energies in Table 1 show further that the vertical stripes are more favorable for charge dynamics. This result, which is not immediately obvious, has however a straightforward origin. Namely, the HF always leads to a large spin polarization since it is the only way to minimize the on-site Coulomb repulsion. Indeed, removal of a $\downarrow$-spin electron at site i leads to relaxation of the $\uparrow$-spin electron energy level at this site. As a consequence, an alternating on-site level shift develops yielding an energetical motivation for the symmetry breaking and forming the AF order.

However, the renormalization of the double occupancy energy involves a strong reduction of the kinetic energy in the $\downarrow$-spin channel between site i and its neighboring sites, as an electron incoming into this site encounters a high energy potential $U\langle n_{i\uparrow}\rangle$. Therefore, in the HF approximation we shall be able to identify dynamically favorable stripe patterns only by

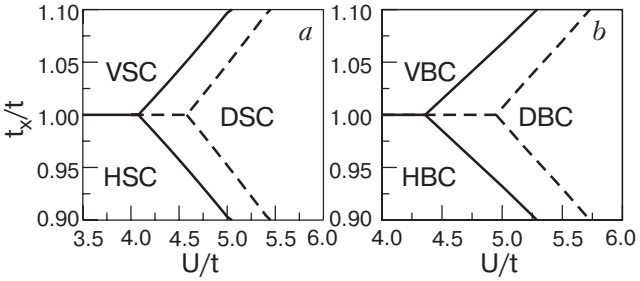

Fig. 6. Phase diagrams for stable: (*a*) site-centered (SC), and (*b*) bond-centered (BC) stripe structures obtained in the anisotropic Hubbard model on a 16×16 cluster for doping $x = 1/8$ (solid lines) and on a 12×12 cluster for $x = 1/6$ (dashed lines). Parameters: $t' = 0$, $V = 0$.

comparing appropriate local magnetization densities. For example, charge fluctuations occur more readily in the VSC stripe geometry presumably due to their greater overall width indicating weaker correlation effects (cf. Fig. 4). This explains their stability at small U where the consequent cost in potential energy E_U becomes insignificant. By contrast, the DSC stripes are narrower having larger hole density along nonmagnetic DWs. Moreover, magnetization density of their nearest neighbor sites is markedly enhanced as compared to the corresponding VSC stripe magnetization, as shown in Fig. 4 and in Table 3. The former also illustrates that the bonds connecting DWs with their nearest neighboring sites perpendicularly to the walls, have the main contribution to the kinetic energy gain, in fact suppressed here by larger spin polarization. Taken together, the above features are reflected in a more localized character of the DSC stripes, with a lower net double occupancy and hence a more favorable on-site energy E_U (cf. Table 1). This clarifies the mechanism of the transition from the VSC to DSC stripes with increasing U.

Table 3. Local hole $\langle n_{hi}\rangle$ and magnetization $\langle S_i^z\rangle$ density of the site-centered stripes shown in Fig. 2, all labeled by decreasing hole density in the x-direction. In parentheses the values for the extended hopping model with $t'/t = -0.15$ are given.

	i	1	2	3	4	5
VSC	$\langle n_{hi}\rangle$	0.364	0.234	0.067	0.014	0.006
		(0.378)	(0.234)	(0.060)	(0.013)	(0.006)
	$\langle S_i^z\rangle$	0.000	0.222	0.348	0.381	0.384
		(0.000)	(0.234)	(0.357)	(0.382)	(0.384)
DSC	$\langle n_{hi}\rangle$	0.388	0.193	0.070	0.032	0.020
		(0.405)	(0.195)	(0.066)	(0.028)	(0.017)
	$\langle S_i^z\rangle$	0.000	0.262	0.352	0.373	0.380
		(0.000)	(0.272)	(0.360)	(0.377)	(0.382)

Turning now to the analogous crossover between the BC stripes, we shall again compare local hole and magnetization densities on and around their DWs. In contrast to the SC case, a VBC stripe phase possesses larger hole density along DWs, as illustrated in Fig. 3 and Table 4, suggesting that it is more localized than the DBC one. Nevertheless, a better renormalization of the double occupancy energy E_U by the latter (cf. Table 1) follows from a stronger spin polarization not only of the DW atoms but also their nearest neighbors (cf. Fig. 3 and Table 4). This enhancement is directly responsible for a substantial reduction of the kinetic energy along bonds joining these atoms. Correspondingly, it accounts for a crossover from the DBC to VBC stripes in the small U regime when the larger kinetic energy gain becomes crucial.

Table 4. The same as in Table 3 but for the bond-centered stripes. VBC stripe is unstable in the extended hopping model with $t'/t = -0.15$ — data in parentheses.

	i	1	2	3	4
VBC	$\langle n_{hi}\rangle$	0.326	0.136	0.030	0.007
	$\langle S_i^z\rangle$	0.118	0.301	0.371	0.384
DBC	$\langle n_{hi}\rangle$	0.314	0.115	0.047	0.023
		(0.323)	(0.110)	(0.046)	(0.021)
	$\langle S_i^z\rangle$	0.145	0.322	0.365	0.378
		(0.155)	(0.333)	(0.368)	(0.380)

We would like to emphasize that the above transition between different types of stripe phases is not an artefact of the HF and occurs also between filled stripes obtained within more realistic approaches including local electron correlations. Indeed, slave-boson studies of the Hubbard model at the doping $x = 1/9$ have established that the transition from the filled VSC to DSC stripe phase appears at the value $U/t \simeq 5.7$, being much higher than that predicted by the HF, which yields $U/t \simeq 3.8$ [14]. In this method, enhanced stability of the VSC stripes follows from an additional variational parameter per each site d_i, reducing the on-site energy without a strong suppression of the kinetic energy. Remarkably, the total energy difference between the vertical SC and BC stripes at both doping levels is comparable to the accuracy of the present calculation. Such degeneracy was also reported in the HF studies of the charge-transfer model [71]. However, when electron correlations are explicitly included the BC stripes are more stable at and above $x = 1/8$ doping [21,79].

3.3. Effect of the next-neighbor hopping t'

We now turn to the effect of a next-neighbor hopping t' on the relative stability of the stripes. There are numerous experimental and theoretical results which support the presence of finite t' in the cuprates. For example, recent slave-boson studies have revealed that the phenomena of the half-filled vertical stripes in LSCO requires a finite next-neighbor hopping $t'/t \simeq -0.2$ [16].

Let us pause now for a moment to clarify the influence of t' on the DOS as well as on the FS using the electronic band which follows from a simple tight-binding model [80],

$$E(\mathbf{k}) = -2t(\cos k_x + \cos k_y) - 4t' \cos k_x \cos k_y \ . \quad (12)$$

By the reduction from the CuO_2 multiband model to an effective single-band model it has been found that $t > 0$ and $t' < 0$ for hole doped system, and $t < 0$ and $t' > 0$ in electron doped system [70]. Although an accidental cancellation of the various contributions results in almost perfect electron-hole symmetry of the nearest neighbor hopping t, the next-neighbor hopping t' asymmetry appears owing to the fact that the dominant contribution to the latter comes from a direct O–O hopping t_{pp} in the case of a hole hopping. On the contrary, an electron hopping follows from a third order Cu → O → O → Cu process, being therefore dominated by the Cu–O hopping element t_{pd}.

In the noninteracting limit the role of t' is to shift the van Hove singularity away from the middle of the band, either to higher or to lower energy depending on its sign [80]. Figure 7 shows the tight-binding DOS, centered at $\omega = 0$ with the condition $\int N(\omega)\omega\, d\omega = 0$, and the occupied states at the doping $x = 1/4$. In the hole-doped case, with the vacuum as the zero electron state, the van Hove singularity lies in the lower part of the band. Conversely, in the case of electron doping, with the vacuum as the zero hole state, the van Hove singularity is shifted towards higher energy part of the band, unoccupied by holes.

Apart from breaking the electron-hole symmetry, the extra parameter t' modifies the shape of the FS of the free electrons and indeed it becomes more consistent with the FS topology seen by ARPES [59,81,82]. In the electron-doped system NCCO, the low-energy spectral weight at the doping $x = 0.04$ is concentrated in small electron pockets around the $(\pm\pi, 0)$ and $(0, \pm\pi)$ points. Upon increasing doping, one observes both the modification of the hole pockets and the emergence of new low-lying spectral weights around $(\pm\pi/2, \pm\pi/2)$. Finally, at $x = 0.15$ the FS pieces evolve into a large holelike curve centered at $M = (\pi, \pi)$. In contrast, it has been observed that in the lightly doped regime($x = 0.03$) doped holes in LSCO enter into the hole pockets around $(\pm\pi/2, \pm\pi/2)$ points [83], implying that the FS is holelike and centered at the M point. However, in the heavy overdoped regime $x = 0.3$ it converts into the electronlike FS around the $\Gamma = (0,0)$ point.

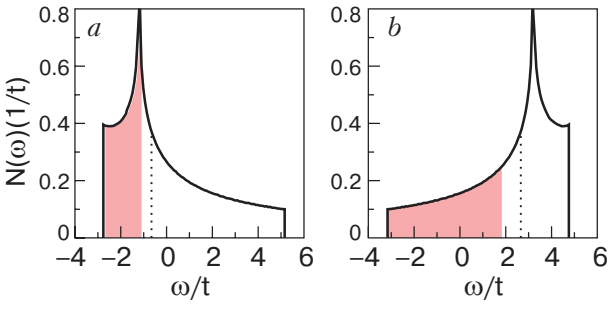

Fig. 7. Effect of the next-neighbor hopping $t'/t = -0.3$ on the noninteracting 2D DOS at the doping $x = 1/4$: (*a*) hole doping ($t = 1$); (*b*) electron doping ($t = -1$). Dotted line shows the Fermi energy in the undoped case, whereas the gray area shows the states occupied by either electrons (*a*) or holes (*b*).

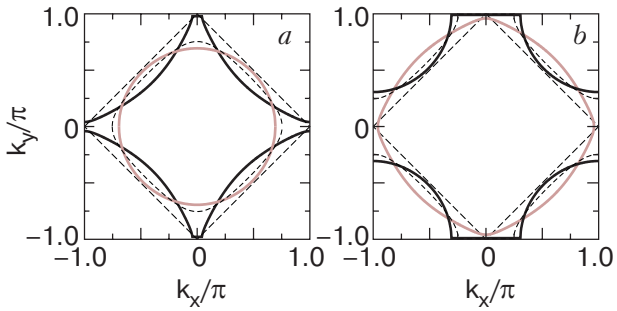

Fig. 8. FS obtained in the tight binding model at the doping $x = 1/4$: (*a*) hole doping with $t = 1$ and: $t' = -0.3$ (black solid line), $t' = 0.3$ (gray solid line), and $t' = 0$ (dashed line); (*b*) electron doping with $t = -1$ and: $t' = 0.3$ (black solid line), $t' = -0.3$ (gray solid line), and $t' = 0$ (dashed line). The long-dashed line in both panels corresponds to the undoped case with $t' = 0$. The excessively large value of $|t'| = 0.3$ as compared to LSCO was chosen only for more clarity of the figure.

Figure 8,*a* shows that the model (12) with $t' = 0$ has a nested square FS at half-filling which becomes electronlike and shrinks around the Γ point upon hole doping. However, negative $t' = -0.3$ removes the FS nesting at half filling, and the FS expands in the $(\pm k, 0)$ and $(0, \pm k)$ directions, while contracts along the nodal $(k, \pm k)$ and $(\pm k, k)$ directions due to a large gradient dE/dk along the latter. Indeed, the eigenenergy map, illustrated in Fig. 9,*a*, has in this case a valleylike character with a minimum at the Γ point. Therefore the FS turns into a holelike one with experimentally observed arcs (cf. Fig. 8,*a*). In contrast, the nearest neighbor hopping t' with the same sign as t interchanges the expansion- and contraction directions which results in the electronlike FS.

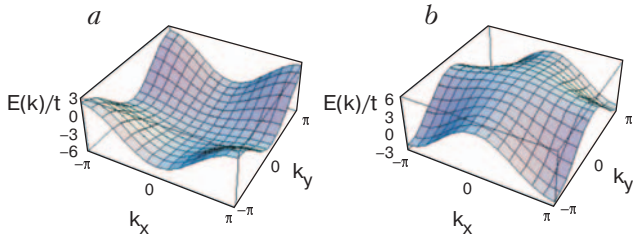

Fig. 9. Eigenenergy maps of the tight-binding model (12) with $t'/t = -0.3$ as obtained for: (*a*) hole doping ($t = 1$); (*b*) electron doping ($t = -1$).

Regarding the electron doped case with $t = -1$, shown in Fig. 8,*b*, positive $t' = 0.3$ (dark solid line) also leads to the appearance of arc segments of the FS and makes it closer to experimental observations. In this case, however, the minimum energy is found at the M point, as illustrated in Fig. 9,*b*. It should be noted in passing that this FS describes the same situation as the one obtained with $t = 1$ and $t' = 0.3$, indicated by the gray solid line in Fig. 8,*a*. In fact, the sign of t is less important and turns out to be equivalent to the (π, π) shift of the momentum without changing the corresponding eigenvalues. Consequently, in order to imitate the effect of hole and electron doping it is sufficient to study the Hamiltonian (1) only below half-filling and the alternation between two regimes is possible by the particle-hole transform,

$$c^{\dagger}_{i\sigma} \to (-1)^{i} c_{i\sigma} , \qquad (13)$$

mapping the model (12) with $t' < 0$ onto the one with $t' > 0$. Therefore, in order to avoid any further confusion concerning the signs of t and t' in Eq. (12), we set hereafter t to be positive; then a negative t' ($t'/t < 0$) corresponds to hole doping, whereas a positive one ($t'/t > 0$) indicates electron doping.

The remarkable differences of the electronic structure due to the broken hole-electron symmetry by t', result in different phase diagrams of LSCO and NCCO. In the former the long-range AF order is already suppressed in the lightly doped regime $x \simeq 0.03$, while in the latter the antiferromagnetism is known to be quite robust at increasing electron doping, hence only *commensurate* spin fluctuations are observed at $x = 0.15$ [68]. The robustness of the commensurate spin fluctuations in the electron doped regime is consistent with the ED studies of the t–t'–J [84,85] and t–t'–t''–J [86,87] models. It is also supported by the conclusion that a negative t' promotes incommensuration at a lower doping level than a positive one, reached using the QMC technique applied to the extended Hubbard model [88]. Finally, the XPS measurements in NCCO show that the chemical potential monotonously increases with electron doping [69], whereas its shift is suppressed in the underdoped region of LSCO [66]. These data have been nicely reproduced in Ref. 86 for both compounds, except for the low doping regime of LSCO where stripes are expected. All these numerical and experimental results indicate that doped electrons might selforganize in a different way than holes do — in the latter case DWs are formed. Nevertheless, stable diagonal stripes with one doped electron per site in a DW have been obtained in the slave-boson studies of a more realistic extended three-band model [73], so the problem is still open.

Turning back to the competition between stripes in a doped system, Fig. 10,*a* shows that negative t' stabilizes the DSC stripes, whereas positive t' favors the VSC ones, within the parameter range where t' does not drive a stripe melting. Analogous crossover from vertical stripes at small $|t'|$ to more complex in shape diagonal ones at $t'/t = -0.1$ and $t'/t = -0.2$ has been found in other HF studies [89]. The explanation is contained in Table 5: negative t' gives a positive kinetic energy contribution, which is much more readily minimized by the diagonal charge configuration. Indeed, despite the solitonic mechanism yielding a noticeable kinetic energy loss due to the transverse hopping $t'/t = -0.15$, the overall kinetic energy loss in the case of DSC stripes along the diagonal (11) and antidiagonal $(1\bar{1})$ directions is smaller than the corresponding one for the VSC stripe. A more careful analysis shows that hole propagation along the DSC stripe results in a contribution having the same sign as t'. However, it is entirely canceled by the ones coming from diagonal bonds of the AF domains so that $E^{x-y}_{t'} = 0$.

One observes further that positive t' reduces the anisotropy between the kinetic energy gains in the x- and y-directions for the VSC stripes, and makes their sum more favorable, while negative t' has the opposite effect. For the DSC stripes the total kinetic energy also follows the same trend. The explanation of these results follows from the reinforcement of stripe order by a negative t' (cf. values in parenthesis in Table 3), which suppresses the hopping contributions, and its smearing out by positive t' where hopping is enhanced. These trends agree with the earlier finding within the DMFT that the VSC stripe phase is destabilized by kink fluctuations [21]. However, this stripe (dis)ordering tendency also leads to a considerably greater change in the Coulomb energy E_U, listed in Table 5, for the DSC than for VSC stripes, which contributes significantly to the predominance of the former structure for negative t'. In fact, it follows from the in-

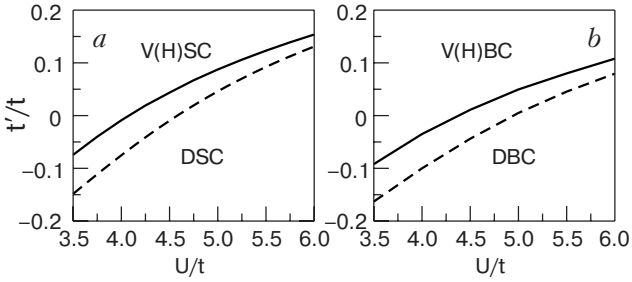

Fig. 10. Phase boundaries for: (*a*) site-centered, and (*b*) bond-centered stripes as obtained in the extended Hubbard model with the next-neighbor hopping t' for doping $x = 1/8$ (solid line) and $x = 1/6$ (dashed line).

Table 5. Energies per site: ground-state energy $E_{\rm tot}$, kinetic energy contributions for the bonds along (10) E_t^x, (01) E_t^y, (11) $E_{t'}^{x-y}$ and $(1\bar{1})$ $E_{t'}^{x+y}$ directions, as well as the potential energy E_U, all normalized per one site, in the extended hopping Hubbard model with $U/t = 5$ and $x = 1/8$. VBC stripe is unstable at $t'/t = -0.15$.

	$t'/t = -0.15$	E_t^x/t	E_t^y/t	$E_{t'}^{x-y}/t$	$E_{t'}^{x+y}/t$	E_U/t	$E_{\rm tot}/t$
VSC	−0.15	−0.6876	−0.5886	0.0140	0.0140	0.4778	−0.7704
DBC	−0.15	−0.6279	−0.6279	0.0000	0.0183	0.4562	−0.7813
DSC	−0.15	−0.6275	−0.6275	0.0000	0.0188	0.4533	−0.7829
DBC	0.15	−0.6442	−0.6442	0.0000	−0.0282	0.4883	−0.8283
DSC	0.15	−0.6437	−0.6437	0.0000	−0.0279	0.4855	−0.8298
VB(S)C	0.15	−0.6612	−0.6372	−0.0169	−0.0169	0.4997	−0.8325

crease of hole density within the nonmagnetic stripes and the magnetization density enhancement within the AF domains (cf. Table 3).

Like their SC counterparts, DBC stripes are also stabilized by negative t' resulting in a phase diagram shown in Fig. 10,*b*. In this case, expelling holes from the AF domains enhances not only magnetization of their atoms but also increases magnetic moment of the hole rich DWs, as illustrated in Table 4. This enhancement must, however, strongly suppress the dominant transverse kinetic energy gain of the VBC stripes. Therefore, the latter are already unstable at $t'/t = -0.15$.

It is worth noting that a finite diagonal hopping t' should directly affect the competition between the *d*-wave pairing correlations and stripes. Indeed, a systematic comparison of stripe and pairing instabilities within the DMRG framework has shown that when the stripes are weakened by positive t', the latter are strongly enhanced due to increasing pair mobility [13]. This effect is accompanied by a simultaneous enhancement of the AF correlations [87]. Conversely, negative t' reinforcing a static stripe order results in the suppression of pair formation in the underdoped region, as found both in the DMRG technique and Variational Monte Carlo (VMC) [90]. However, the enhanced pairing correlation, attributed to the change of the FS topology in LSCO, has been obtained in the optimally doped and overdoped regimes [91].

3.4. Effect of the nearest-neighbor Coulomb interaction V

We now investigate the changes in the stripe stability due to either repulsive ($V > 0$) or attractive ($V < 0$) nearest-neighbor Coulomb interaction, which give the phase boundaries between the VSC and DSC stripe phases shown in Fig. 1,*a*. We have found that realistic repulsive V favors the latter. The tendency towards the DSC stripe formation at $V > 0$ is primarily due to a large difference between charge densities at the atoms of the DW itself and at all their nearest-neighbor sites, a situation which is avoided in the case of VSC stripe phases (cf. Fig. 2). Consequently, the former optimize better the repulsive potential energy component E_V, as shown by the data reported in Table 4. Similarly, the fact that the nearest-neighbor interaction V is well minimized only by inhomogeneous charge densities makes the DBC stripe phase more favorable than the VBC one, as shown in Fig. 11,*b*. While this is also the leading mechanism for both diagonal stripe suppression at $V < 0$, the asymmetry of the curve in Fig. 11 arises from the fact that the lower U values at the transition favor the higher kinetic energy contributions available for the vertical stripes.

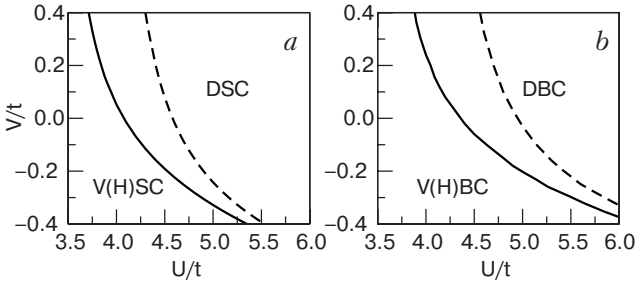

Fig. 11. Phase diagrams for the site-centered (*a*) and bond-centered (*b*) stripes obtained in the extended Hubbard model with the nearest-neighbor Coulomb interaction V for doping $x = 1/8$ (solid line) and $x = 1/6$ (dashed line).

Table 6. Energies per site: ground-state energy $E_{\rm tot}$, kinetic energy (E_t^x, E_t^y) and potential energy (E_U, E_V) components in the extended Hubbard model with the nearest-neighbor Coulomb interaction V for $U/t = 5$ and $x = 1/8$.

	V/t	E_t^x/t	E_t^y/t	E_U/t	E_V/t	$E_{\rm tot}/t$
DBC	−0.4	−0.6322	−0.6322	0.4626	−0.6194	−1.4212
DSC	−0.4	−0.6319	−0.6319	0.4602	−0.6193	−1.4229
VB(S)C	−0.4	−0.6655	−0.6083	0.4749	−0.6251	−1.4240
VB(S)C	0.4	−0.6838	−0.6214	0.5063	0.6207	−0.1782
DBC	0.4	−0.6424	−0.6424	0.4829	0.6176	−0.1843
DSC	0.4	−0.6412	−0.6412	0.4789	0.6171	−0.1864

However, it has been argued based on the results obtained using the SBA that an increasing repulsive interaction V favors half-filled vertical stripes, hence the latter take over at $V/t \simeq 0.1$ in the parameter regime of $x = 1/8$ and $U/t = 10$ [15]. This finding could naturally explain the appearance of filled diagonal stripes in the nickelates, provided that they were characterized by a small V term, and the stability of the half-filled vertical ones in the Nd-codoped cuprates due to possibly larger value of V. It is also worth mentioning other HF [92] and variational [93] studies in which a variety of intriguing stripe phases, coexisting at $V/t \simeq 1.5$ with charge order, has been found in a broad doping region.

3.5. Effect of the lattice deformations

So far, we have demonstrated that a finite anisotropy of the transfer integral t can tip the balance between vertical and diagonal stripes. Here we will show that such anisotropy naturally emerges in a doped system with DWs, described by a single-band Peierls-Hubbard Hamiltonian,

$$H = -\sum_{ij\sigma} t_{ij}(u_{ij}) c^{\dagger}_{i\sigma} c_{j\sigma} + U \sum_i n_{i\uparrow} n_{i\downarrow} + \frac{1}{2} K \sum_{\langle ij \rangle} u_{ij}^2 \ . \tag{14}$$

In this model we keep only the leading term and assume a linear dependence of the nearest neighbor hopping element t_{ij} on the lattice displacements u_{ij},

$$t_{ij}(u_{ij}) = t_0(1 + \alpha u_{ij}) \ . \tag{15}$$

Furthermore, we include the elastic energy $\propto K$ which allows to investigate the stability of the system with respect to a given lattice deformation and to determine the equilibrium configuration. For convenience, we parametrize the electron-lattice coupling

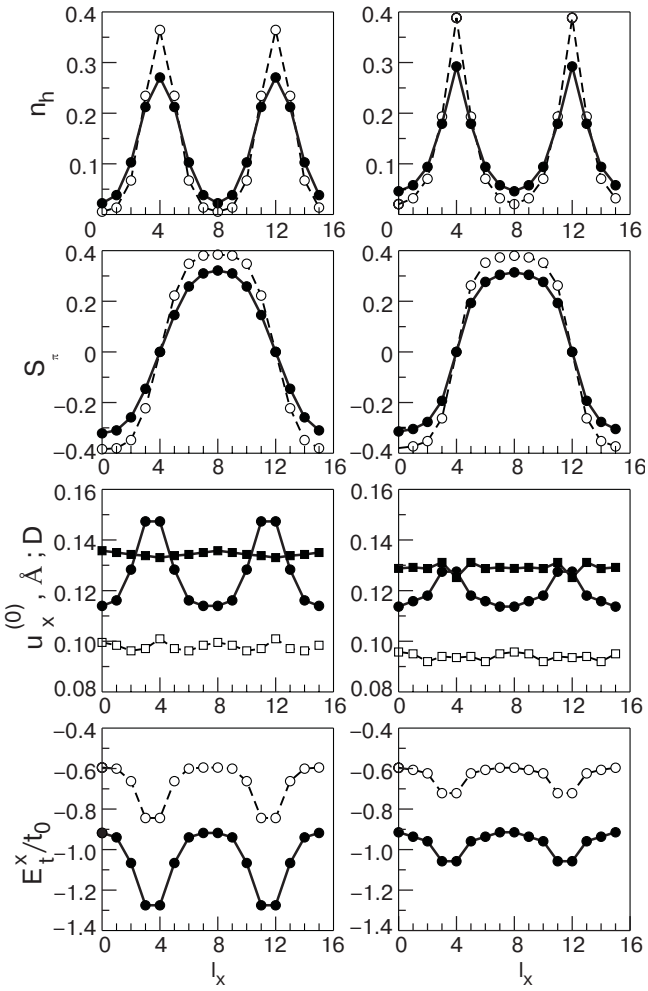

Fig. 12. Local hole $n_h(l_x)$ (top) and magnetization $S_\pi(l_x)$ (second row) density; fractional change of the length for the bonds to the right nearest-neighbor along the x-direction $u_x^{(0)}$ (circles) and double occupancy $D(l_x)$ (squares) (third row), as well as the kinetic energy $E_t^x(l_x)$ projected on the bonds in the x-direction (bottom) of the VSC (left) and DSC (right) stripe phases, as obtained in the Peierls-Hubbard model (14) with $U/t = 5$, $\lambda = 0.5$ and $x = 1/8$ (filled symbols). For comparison the results obtained with $\lambda = 0$ are shown by open symbols.

with a single quantity, $\lambda = \alpha^2 t_0/K$, with the parameter values $K/t_0 = 18$ and $\alpha = 3$ assumed following the earlier HF studies [26]. As previously, we focus on the doping $x = 1/8$ ($x = 1/6$) and present the results of calculations performed on 16×16 (12×12) clusters, respectively, with periodic boundary conditions. These calculations have shown that such clusters give the most stable filled stripe solutions for the selected doping levels. The model (14) was solved self-consistently in real space within the HF (2). Thereby, we used an approximate saddle-point formula for the equilibrium relation between the actual deformation

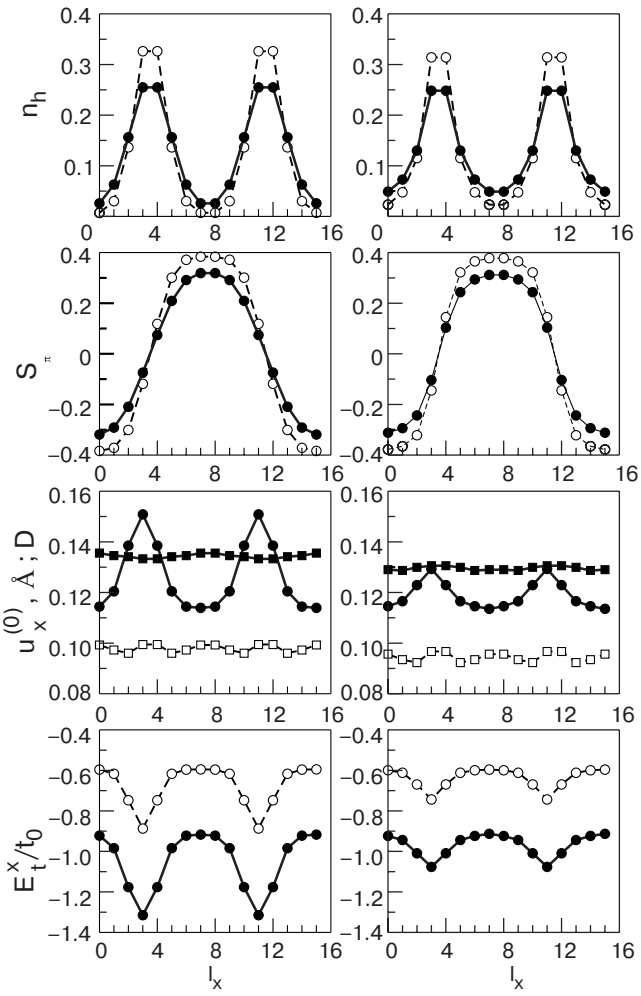

Fig. 13. The same as in Fig. 12 but for the bond-centered stripes.

u_{ij} of a given bond and the bond-charge density $\langle c^\dagger_{i\sigma} c_{j\sigma}\rangle$,

$$u_{ij}^{(0)} \simeq \frac{\alpha t_0}{K} \sum_\sigma \langle c^\dagger_{i\sigma} c_{j\sigma} + \text{h.c.}\rangle\,, \qquad (16)$$

being a consequence of the linearity assumption in Eq. (15).

Quite generally, it is a widely spread out belief that inhomogeneous states at finite doping are very sensitive to small changes of λ, supported both by the HF [94,95] and ED studies [96]. Further, it has been shown that the electron-lattice interaction favors DW solutions over other possible phases, such as isolated polarons or bipolarons [26]. Therefore, a complete discussion of the stripe phase stability in correlated oxides has to include the coupling to the lattice.

We turn now to the most important aspect of this Section. Figures 12 and 13 illustrate the effect of the finite electron-lattice coupling $\lambda = 0.5$ on the SC and BC stripes, respectively. Both figures give a clear demonstration that, in contrast to the hopping anisotropy ε_t (7) discussed above, finite λ markedly modifies both the local hole density (8) and modulated magnetization (9) [cf. also Table 3 with 7 (SC stripes) and Table 4 with 8 (BC stripes)]. Basically, the influence of λ resembles the effect of positive t', smearing out the stripe order by ejecting holes from the DWs, being however much stronger. In fact, hole delocalization not only suppresses the magnetization within the AF domains, but also noticeably quenches magnetic moments of the BC domain walls. These trends can be understood by considering energy increments: the kinetic E_t, on-site E_U, and elastic energy E_K, as explained below.

Table 7. Local hole $\langle n_{\text{h}i}\rangle$ and magnetization $\langle S_i^z\rangle$ density at nonequivalent atoms of the SC stripe phases, all labeled by decreasing hole density in the x-direction, in the Peierls-Hubbard model on a 16×16 cluster with $U/t = 5$, $\lambda = 0.5$ and $x = 1/8$.

	i	1	2	3	4	5
VSC	$\langle n_{hi}\rangle$	0.270	0.212	0.103	0.038	0.022
	$\langle S_i^z\rangle$	0.000	0.146	0.259	0.310	0.321
DSC	$\langle n_{hi}\rangle$	0.292	0.179	0.094	0.058	0.046
	$\langle S_i^z\rangle$	0.000	0.193	0.277	0.305	0.314

Table 8. The same as in Table 7 but for the BC stripe phases.

	i	1	2	3	4
VBC	$\langle n_{hi}\rangle$	0.255	0.156	0.063	0.026
	$\langle S_i^z\rangle$	0.074	0.209	0.291	0.319
DBC	$\langle n_{hi}\rangle$	0.248	0.130	0.073	0.049
	$\langle S_i^z\rangle$	0.103	0.243	0.294	0.312

One should realize that a system described by the Hamiltonian (14) might be unstable towards lattice deformations only if the covalency increase is large enough to compensate both the E_U and E_K energy cost. Without the electron-lattice coupling, a compromise solution is mainly reached by developing a strong magnetic order in the AF domains, where a possible kinetic energy gain is irrelevant, and by forming nonmagnetic or weakly magnetic DWs with large hole density. As we have already shown, transverse charge fluctuations around the DWs yield the leading kinetic energy contribution. However, enhanced covalency and mixing of the lower $\sim\varepsilon_d$ and higher $\sim\varepsilon_d + U$ energy states between a DW and the surrounding sites partly delocalize these states and increase double occupancy,

$$D(l_x) = \langle n_{(l_x,0),\uparrow} n_{(l_x,0),\downarrow} \rangle \,. \qquad (17)$$

Indeed, in the $\lambda = 0$ case, double occupancy $D(l_x)$ reaches its maximum at the DWs, as illustrated in Figs. 12 and 13. The only exception is the DSC stripe phase (right panels of Fig. 12) with the largest $D(l_x)$ in the AF domains. As a consequence, the latter is the most localized one with the smallest kinetic energy gain (cf. Table 1).

The situation changes when turning on the electron-lattice coupling. When the electrons couple to the lattice ($\lambda \neq 0$), the bonds contract, and the saddle point values of the distortions (16): $u_{ij}^{(0)} = \langle u_{ij} \rangle$ along (10) and (01) direction, respectively, are finite. However, a nonuniform charge distribution results in a different bondlength in the cluster. This is illustrated in Figs. 12 and 13 showing a fractional change of the length for the bonds to the right nearest-neighbor along the x-direction $u_x^{(0)}$ (third row). Although the values of $u_{ij}^{(0)}$ in the AF domains are also substantial, the largest lattice deformations $\sim \langle c_{i\sigma}^{\dagger} c_{j\sigma} \rangle$ appear either on the bonds connecting atoms of the DWs with their nearest neighbors (cf. Fig. 12), or on the bonds which join two atoms of the bond-centered DWs (cf. Fig. 13). Accordingly, a strengthening nearest neighbor hopping (15) enables a larger kinetic energy gain on these bonds (cf. bottom of Figs. 12 and 13).

Table 9. Ground-state energy $E_{\rm tot}$ per site, kinetic energy (E_t^x, E_t^y) and potential energy (E_U, E_K) components, as obtained in the Peierls-Hubbard model. Parameters: $U/t = 5$, $\lambda = 0.5$, and $x = 1/8$.

	E_t^x/t	E_t^y/t	E_U/t	E_K/t	$E_{\rm tot}/t$
DBC	−0.9679	−0.9679	0.6478	0.2548	−1.0332
DSC	−0.9670	−0.9670	0.6450	0.2544	−1.0346
VB(S)C	−1.0496	−0.9248	0.6719	0.2638	−1.0387

As expected, the increasing covalency is accompanied by partial quenching of magnetic moments. In order to appreciate this tendency, let us consider a site in the AF domain with larger density of ↑-spin electrons (at A sublattice). Once the magnetization is reduced, the corresponding ↑-spin energy level which belongs to the lower Hubbard band is pushed upwards, and the ↓-spin of the upper Hubbard band goes down. As a result, the locally raised ↑-spin state becomes stronger mixed with ↓-spin states at the surrounding sites of B sublattice, and simultaneously bond-charge density increases. At the same time, electrons, jumping forth and back between the central site with the ↑-spin polarization and its nearest neighbors with the ↓-spin one, enhance considerably double occupancy $D(l_x)$, as shown in Figs. 12 and 13. This weakens the stripe order and results in a more uniform distribution of $D(l_x)$. Of course, the increase of the elastic energy and concomitant enhancement of the on-site energy, both owing to finite bond contractions (16), is compensated by the kinetic energy gain and the total energy is lowered (cf. Tables 1 and 9).

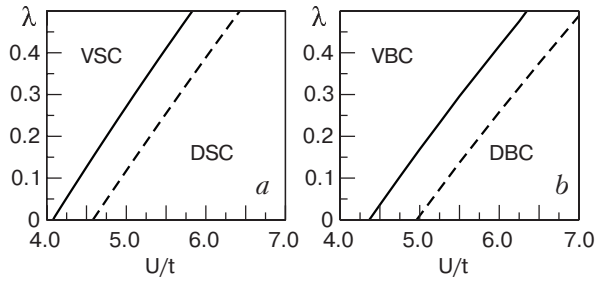

Fig. 14. Phase diagrams for site-centered (*a*) and bond-centered (*b*) stripe structures as calculated from the Peierls-Hubbard model for doping $x = 1/8$ (solid line) and $x = 1/6$ (dashed line).

We close this Section with the phase diagrams shown in Fig. 14. They were obtained by varying U and the coefficient α, while maintaining constant $K/t_0 = 18$. The increased stability of vertical stripes follows from the relative stronger enhancement of the local hopping elements (15) (and consequently larger gain of the kinetic energy), especially on the bonds in the direction perpendicular to the DWs itself.

4. Summary

In summary, we have shown that a competition between magnetic energy of interacting almost localized electrons and the kinetic energy of holes created by doping leads to the formation of new type of coexisting charge and spin order — the stripe phases. We have shown that vertical (horizontal) and diagonal stripes dominate the behavior of the charge structures formed by doping the antiferromagnet away from half filling, using the solutions obtained for the Hubbard model within the HF approximation in the physically interesting regime of the Coulomb interaction. The detailed charge distribution and the type of stripe order depend on the ratio U/t, on the value of the next-neighbor hopping t', and on the nearest-neighbor Coulomb interaction V. We have also shown that a strong electron-lattice coupling might be responsible for the appearance of the vertical stripes observed in the superconducting cuprates at $x = 1/8$.

Altogether, although some experimentally observed trends could be reproduced already in the HF approach, the presented results indicate that strong electron correlations play a crucial role in the stripe

phases and have to be included for a more quantitative analysis. Further progress both in the experiment and in the theory is necessary to establish the possible role of stripes in the phenomenon of high temperature superconductivity.

M. Raczkowski was supported by a Marie Curie fellowship of the European Community program under number HPMT2000-141. This work was supported by the the Polish Ministry of Scientific Research and Information Technology, Project No. 1 P03B 068 26, and by the Ministére Français des Affaires Etrangéres under POLONIUM 09294VH.

1. J.G. Bednorz and K.A. Müller, *Z. Phys.* **B64**, 189 (1986).
2. E.W. Carlson, V.J. Emery, S.A. Kivelson, D. Orgad, *Concepts in High Temperature Superconductivity* in: *The Physics of Conventional and Unconventional Superconductors*, K.H. Bennemann and J.B. Ketterson (eds.), Springer-Verlag (2002), *cond-mat/0206217*.
3. J. Zaanen and O. Gunnarsson, *Phys. Rev.* **B40**, 7391 (1989).
4. D. Poilblanc and T.M. Rice, *Phys. Rev.* **B39**, 9749 (1989).
5. H.J. Schulz, *J. Phys. (Paris)* **50**, 2833 (1989); *Phys. Rev. Lett.* **64**, 1445 (1990).
6. M. Kato, K. Machida, H. Nakanishi, and M. Fujita, *J. Phys. Soc. Jpn.* **59**, 1047 (1990).
7. M. Inui and P.B. Littlewood, *Phys. Rev.* **B44**, 4415 (1991).
8. O. Zachar, S.A. Kivelson, and V.J. Emery, *Phys. Rev.* **B57** 1422 (1998); J. Zaanen, *Physica* **C317**, 217 (1999).
9. S.A. Kivelson and V.J. Emery, *Synth. Metals* **80**, 151 (1996).
10. U. Löw, V.J. Emery, K. Fabricius, and S.A. Kivelson, *Phys. Rev. Lett.* **72**, 1918 (1994).
11. C.N.A. van Duin and J. Zaanen, *Phys. Rev. Lett.* **80**, 1513 (1998).
12. S.R. White and D.J. Scalapino, *Phys. Rev. Lett.* **80**, 1272 (1998).
13. S.R. White and D.J. Scalapino, *Phys. Rev.* **B60**, R753 (1999).
14. G. Seibold, E. Sigmund, and V. Hizhnyakov, *Phys. Rev.* **B57**, 6937 (1998).
15. G. Seibold, C. Castellani, C. Di Castro, and M. Grilli, *Phys. Rev.* **B58**, 13506 (1998).
16. G. Seibold and J. Lorenzana, *Phys. Rev.* **B69**, 134513 (2004).
17. D. Góra, K. Rościszewski, and A.M. Oleś, *Phys. Rev.* **B60**, 7429 (1999).
18. T. Tohyama, S. Nagai, Y. Shibata, and S. Maekawa, *Phys. Rev. Lett.* **82**, 4910 (1999).
19. P. Wróbel and R. Eder, *Phys. Rev.* **B62**, 4048 (2000).
20. M. Fleck, A.I. Lichtenstein, E. Pavarini, and A.M. Oleś, *Phys. Rev. Lett.* **84**, 4962 (2000).
21. M. Fleck, A.I. Lichtenstein, and A.M. Oleś, *Phys. Rev.* **B64**, 134528 (2001).
22. M.G. Zacher, R. Eder, E. Arrigoni, and W. Hanke, *Phys. Rev. Lett.* **85**, 2585 (2000); *Phys. Rev.* **B65**, 045109 (2002).
23. F. Becca, L. Capriotti, and S. Sorella, *Phys. Rev. Lett.* **87**, 167005 (2001).
24. J. Riera, *Phys. Rev.* **B64**, 104520 (2001).
25. M. Raczkowski, R. Frésard, and A.M. Oleś, *Physica* **B359–361**, 780 (2005).
26. J. Zaanen and A.M. Oleś, *Ann. Phys. (Leipzig)* **5**, 224 (1996).
27. S.A. Kivelson, I.P. Bindloss, E. Fradkin, V. Oganesyan, J.M. Tranquada, A. Kapitulnik, and C. Howald, *Rev. Mod. Phys.* **75**, 1201 (2003).
28. A. Damascelli, Z. Hussain, and Z.-X. Shen, *Rev. Mod. Phys.* **75**, 473 (2003).
29. J.M. Tranquada, B.J. Sternlieb, J.D. Axe, Y. Nakamura, and S. Uchida, *Nature* **375**, 561 (1995).
30. J.M. Tranquada, J.D. Axe, N. Ichikawa, Y. Nakamura, S. Uchida, and B. Nachumi, *Phys. Rev.* **B54**, 7489 (1996).
31. N. Ichikawa, S. Uchida, J.M. Tranquada, T. Niemöller, P.M. Gehring, S.-H. Lee, and J.R. Schneider, *Phys. Rev. Lett.* **85**, 1738 (2000).
32. J.M. Tranquada, J.D. Axe, N. Ichikawa, A.R. Moodenbaugh, Y. Nakamura, and S. Uchida, *Phys. Rev. Lett.* **78**, 338 (1997).
33. P.M. Singer, A.W. Hunt, A.F. Cederström, and T. Imai, *Phys. Rev.* **B60**, 15345 (1999).
34. S. Wakimoto, R.J. Birgeneau, Y. Fujimaki, N. Ichikawa, T. Kasuga, Y.J. Kim, K.M. Kojima, S.-H. Lee, H. Niko, J.M. Tranquada, S. Uchida, and M. von Zimmermann, *Phys. Rev.* **B67**, 184419 (2003).
35. G.B. Teitel'baum, B. Büchner, and H. de Gronckel, *Phys. Rev. Lett.* **84**, 2949 (2000).
36. H.-H. Klauss, W. Wagener, M. Hillberg, W. Kopmann, H. Walf, F.J. Litterst, M. Hücker, and B. Büchner, *Phys. Rev. Lett.* **85**, 4590 (2000).
37. M. Fujita, H. Goka, K. Yamada, and M. Matsuda, *Phys. Rev. Lett.* **88**, 167008 (2002).
38. H. Kimura, Y. Noda, H. Goka, M. Fujita, K. Yamada, M. Mizumaki, N. Ikeda, and H. Ohsumi, *Phys. Rev.* **B70**, 134512 (2004).
39. M. Fujita, H. Goka, K. Yamada, J.M. Tranquada, and L.P. Regnault, *Phys. Rev.* **B70**, 104517 (2004).
40. K. Yamada, C.H. Lee, K. Kurahashi, J. Wada, S. Wakimoto, S. Ueki, H. Kimura, Y. Endoh, S. Hosoya, G. Shirane, R.J. Birgeneau, M. Greven, M.A. Kastner, and Y.J. Kim, *Phys. Rev.* **B57**, 6165 (1998).
41. S. Wakimoto, G. Shirane, Y. Endoh, K. Hirota, S. Ueki, K. Yamada, R.J. Birgeneau, M.A. Kastner, Y.S. Lee, P.M. Gehring, and H.S. Lee, *Phys. Rev.* **B60**, R769 (1999).
42. S. Wakimoto, R.J. Birgeneau, M.A. Kastner, Y.S. Lee, R. Erwin, P.M. Gehring, S.H. Lee, M. Fujita, K. Yamada, Y. Endoh, K. Hirota, and G. Shirane, *Phys. Rev.* **B61**, 3699 (2000).
43. M. Fujita, K. Yamada, H. Hiraka, P.M. Gehring, S.H. Lee, S. Wakimoto, and G. Shirane, *Phys. Rev.* **B65**, 064505 (2002).

44. N. Hasselmann, A.H. Castro Neto, and C. Morais Smith, *Phys. Rev.* **B69**, 014424 (2004).
45. M. Matsuda, Y.S. Lee, M. Greven, M.A. Kastner, R.J. Birgeneau, K. Yamada, Y. Endoh, P. Bóni, S.-H. Lee, S. Wakimoto, and G. Shirane, *Phys. Rev.* **B61**, 4326 (2000).
46. M. Matsuda, M. Fujita, K. Yamada, R.J. Birgeneau, M.A. Kastner, H. Hiraka, Y. Endoh, S. Wakimoto, and G. Shirane, *Phys. Rev.* **B62**, 9148 (2000).
47. M. Matsuda, M. Fujita, K. Yamada, R.J. Birgeneau, Y. Endoh, and G. Shirane, *Phys. Rev.* **B65**, 134515 (2002).
48. A.W. Hunt, P.M. Singer, K.R. Thurber, and T. Imai, *Phys. Rev. Lett.* **82**, 4300 (1999).
49. Y. Ando, K. Segawa, S. Komiya, and A.N. Lavrov, *Phys. Rev. Lett.* **88**, 137005 (2002).
50. M. Dumm, S. Komiya, Y. Ando, and D.N. Basov, *Phys. Rev. Lett.* **91**, 077004 (2003).
51. B.O. Wells, Y.S. Lee, M.A. Kastner, R.J. Christanson, R.J. Birgeneau, K. Yamada, Y. Endoh, and G. Shirane, *Science* **277**, 1067 (1997); Y.S. Lee, R.J. Birgeneau, M.A. Kastner, Y. Endoh, S. Wakimoto, K. Yamada, R.W. Erwin, S.-H. Lee, and G. Shirane, *Phys. Rev.* **B60**, 3643 (1999).
52. K. Hirota, K. Yamada, I. Tanaka, and H. Kojima, *Physica* **B241**, 817 (1998).
53. H. Kimura, K. Hirota, H. Matsushita, K. Yamada, Y. Endoh, S.-H. Lee, C.F. Majkrzak, R. Erwin, G. Shirane, M. Greven, Y.S. Lee, M.A. Kastner, and R.J. Birgeneau, *Phys. Rev.* **B59**, 6517 (1999); J.M. Tranquada, N. Ichikawa, K. Kakurai, and S. Uchida, *J. Phys. Chem. Solids* **60**, 1019 (1999).
54. P. Dai, H.A. Mook, R.D. Hunt, and F. Dovǧan, *Phys. Rev.* **B63**, 054525 (2001).
55. H.A. Mook, P. Dai, and F. Dovǧan, *Phys. Rev. Lett.* **88**, 097004 (2002).
56. H.A. Mook and B.C. Chakoumakos, *J. Supercond.* **10**, 389 (1997).
57. C. Howald, H. Eisaki, N. Kaneko, M. Greven, and A. Kapitulnik, *Phys. Rev.* **B67**, 014533 (2003); A. Fang, C. Howald, N. Kaneko, M. Greven, A. Kapitulnik, *Phys. Rev.* **B70**, 214514 (2004).
58. A. Ino, C. Kim, M. Nakamura, T. Yoshida, T. Mizokawa, Z.-X. Shen, A. Fujimori, T. Kakeshita, H. Eisaki, and S. Uchida, *Phys. Rev.* **B62**, 4137 (2000).
59. A. Ino, C. Kim, M. Nakamura, T. Yoshida, T. Mizokawa, A. Fujimori, Z.-X. Shen, T. Kakeshita, H. Eisaki, and S. Uchida, *Phys. Rev.* **B65**, 094504 (2002).
60. A. Ino, T. Mizokawa, K. Kobayashi, A. Fujimori, T. Sasagawa, T. Kimura, K. Kishio, K. Tamasaku, H. Eisaki, and S. Uchida, *Phys. Rev. Lett.* **81**, 2124 (1998).
61. X.J. Zhou, P. Bogdanov, S.A. Kellar, T. Noda, H. Eisaki, S. Uchida, Z. Hussain, and Z.-X. Shen, *Science* **286**, 268 (1999).
62. X.J. Zhou, T. Yoshida, S.A. Kellar, P.V. Bogdanov, E.D. Lu, A. Lanzara, M. Nakamura, T. Noda, T. Kakeshita, H. Eisaki, S. Uchida, A. Fujimori, Z. Hussain, and Z.-X. Shen, *Phys. Rev. Lett.* **86**, 5578 (2001).
63. M.I. Salkola, V.J. Emery, and S.A. Kivelson, *Phys. Rev. Lett.* **77**, 155 (1996).
64. V.J. Emery, S.A. Kivelson, and O. Zachar, *Phys. Rev.* **B56**, 6120 (1997).
65. P. Wróbel, A. Maciąg, and R. Eder, *cond-mat/0408703*.
66. A.Ino, T. Mizokawa, A. Fujimori, K. Tamasaku, H. Eisaki, S. Uchida, T. Kimura, T. Sasagawa, and K. Kishio, *Phys. Rev. Lett.* **79**, 2101 (1997).
67. T. Noda, H. Eisaki, and S. Uchida, *Science* **286**, 265 (1999).
68. K. Yamada, K. Kurahashi, T. Uefuji, M. Fujita, S. Park, S.-H. Lee, and Y. Endoh, *Phys. Rev. Lett.* **90**, 137004 (2003).
69. N. Harima, J. Matsuno, A. Fujimori, Y. Onose, Y. Taguchi, and Y. Tokura, *Phys. Rev.* **B64**, 220507 (2001).
70. L.F. Feiner, J.H. Jefferson and R. Raimondi, *Phys. Rev.* **B53**, 8751 (1996).
71. T. Mizokawa and A. Fujimori, *Phys. Rev.* **B56**, 11920 (1997).
72. Z.G. Yu, J. Zang, J.T. Gammel, and A.R. Bishop, *Phys. Rev.* **B57**, R3241 (1998).
73. A. Sadori and M. Grilli, *Phys. Rev. Lett.* **84**, 5375 (2000).
74. J. Lorenzana and G. Seibold, *Phys. Rev. Lett.* **89**, 136401 (2002).
75. A. Büchner, M. Breuer, A. Freimuth, and A.P. Kampf, *Phys. Rev. Lett.* **73**, 1841 (1994).
76. A. Normand and A.P. Kampf, *Phys. Rev.* **B64**, 024521 (2001).
77. A.P. Kampf, D.J. Scalapino, and S.R. White, *Phys. Rev.* **B64**, 052509 (2001).
78. J.M. Tipper and K.J.E. Vos, *Phys. Rev.* **B67**, 144511 (2003).
79. P. Wróbel, A. Maciąg, and R. Eder, *J. Phys. Condens. Matter* **18**, 1249 (2006).
80. M. Fleck, A.M. Oleś, and L. Hedin, *Phys. Rev.* **B56**, 3159 (1997).
81. A.M. King, Z.-X. Shen, D.S. Dessau, B.O. Wells, W.E. Spicer, A.J. Arko, D.S. Marshall, J. DiCarlo, A.G. Loeser, C.H. Park, E.R. Ratner, J.L. Peng, Z.Y. Li, and R.L. Greene, *Phys. Rev. Lett.* **70**, 3159 (1993).
82. N.P. Armitage, F. Ronning, D.H. Lu, C. Kim, A. Damascelli, K.M. Shen, D.L. Feng, H. Eisaki, Z.-X. Shen, P.K. Mang, N. Kaneko, M. Greven, Y. Onose, Y. Taguchi, and Y. Tokura, *Phys. Rev. Lett.* **88**, 257001 (2002).
83. T. Yoshida, X.J. Zhou, T. Sasagawa, W.L. Yang, P.V. Bogdanov, A. Lanzara, Z. Hussain, T. Mizokawa, A. Fujimori, H. Eisaki, Z.-X. Shen, T. Kakeshita, and S. Uchida, *Phys. Rev. Lett.* **91**, 027001 (2003).
84. T. Tohyama and S. Maekawa, *Phys. Rev.* **B49**, 3596 (1994).
85. R.J. Gooding, K.J. E. Vos, and P.W. Leung, *Phys. Rev.* **B50**, 12866 (1994).

86. T. Tohyama and S. Maekawa, *Phys. Rev.* **B67**, 092509 (2003).
87. T. Tohyama, *Phys. Rev*. **B70**, 174517 (2004).
88. A. Duffy and A. Moreo, *Phys. Rev.* **B52**, 15607 (1995).
89. A. Normand and A.P. Kampf, *Phys. Rev.* **B65**, 020509 (2002).
90. A. Himeda, T. Kato, and M. Ogata, *Phys. Rev. Lett.* **88**, 117001 (2002).
91. A.T. Shih, T.K. Lee, R. Eder, C.-Y. Mou, and Y.C. Chen, *Phys. Rev. Lett*. **92**, 227002 (2004).
92. T. Kato and M. Kato, *J. Phys. Soc. Jpn.* **69**, 3972 (2000).
93. K. Rościszewski and A.M. Oleś, *J. Phys.: Condens. Matter* **15**, 8363 (2003).
94. K. Yonemitsu, A.R. Bishop, and J. Lorenzana, *Phys. Rev. Lett.* **69**, 965 (1992); *Phys. Rev.* **B47**, 8065 (1993); *ibid*. **B47**, 12059 (1993).
95. M. Raczkowski and A.M. Oleś, *Physica* **C387**, 82 (2003).
96. A. Dobry, A. Greco, J. Lorenzana, and J. Riera, *Phys. Rev.* **B49**, 505 (1994); J. Lorenzana and A. Dobry *Phys. Rev*. **B50**, 16094 (1994).